APL Materials

RESEARCH ARTICLE | NOVEMBER 13 2023

Growth of β-Ga_2O_3 and ϵ/κ-Ga_2O_3 on AlN(0001) by molecular-beam epitaxy

Sushma Raghuvansy; Jon P. McCandless; Marco Schowalter; Alexander Karg; Manuel Alonso-Orts; Martin S. Williams; Christian Tessarek; Stephan Figge; Kazuki Nomoto; Huili Grace Xing; Darrell G. Schlom; Andreas Rosenauer; Debdeep Jena; Martin Eickhoff; Patrick Vogt

Check for updates

APL Mater. 11, 111113 (2023)
https://doi.org/10.1063/5.0174373

CrossMark

View Online

Export Citation

AMERICAN ELEMENTS
THE ADVANCED MATERIALS MANUFACTURER
The Next Generation of Material Science Catalogs
Now Invent.
www.americanelements.com

APL Materials ARTICLE pubs.aip.org/aip/apm

Growth of β-Ga_2O_3 and ϵ/κ-Ga_2O_3 on AlN(0001) by molecular-beam epitaxy

Cite as: APL Mater. 11, 111113 (2023); doi: 10.1063/5.0174373
Submitted: 30 August 2023 • Accepted: 24 October 2023 •
Published Online: 13 November 2023

View Online

Export Citation
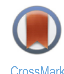
CrossMark

Sushma Raghuvansy,[1,a)] Jon P. McCandless,[1,2] Marco Schowalter,[1] Alexander Karg,[1] Manuel Alonso-Orts,[1,3] Martin S. Williams,[1] Christian Tessarek,[1] Stephan Figge,[1] Kazuki Nomoto,[2] Huili Grace Xing,[2,4,5] Darrell G. Schlom,[4,5,6] Andreas Rosenauer,[1,3] Debdeep Jena,[2,4,5] Martin Eickhoff,[1,3] and Patrick Vogt[1,4,b)]

AFFILIATIONS

[1] Institute of Solid-State Physics, University of Bremen, Otto-Hahn-Allee 1, 28359 Bremen, Germany
[2] School of Electrical and Computer Engineering, Cornell University, Ithaca, New York 14853, USA
[3] MAPEX Center for Materials and Processes, University of Bremen, 28359 Bremen, Germany
[4] Department of Material Science and Engineering, Cornell University, Ithaca, New York 14853, USA
[5] Kavli Institute at Cornell for Nanoscale Science, Cornell University, Ithaca, New York 14853, USA
[6] Leibniz-Institut für Kristallzüchtung, Max-Born-Str. 2, 12489 Berlin, Germany

[a)] **Author to whom correspondence should be addressed:** raghuvan@uni-bremen.de
[b)] **Electronic mail:** pvogt@uni-bremen.de

ABSTRACT

The heteroepitaxial growth and phase formation of Ga_2O_3 on Al-polar AlN(0001) templates by molecular-beam epitaxy (MBE) are studied. Three different MBE approaches are employed: (i) conventional MBE, (ii) *suboxide* MBE (*S*-MBE), and (iii) metal-oxide-catalyzed epitaxy (MOCATAXY). We grow phase-pure β-$Ga_2O_3(\bar{2}01)$ and phase-pure ϵ/κ-Ga_2O_3(001) with smooth surfaces by *S*-MBE and MOCATAXY. Thin film analysis shows that the crystallographic and surface features of the β-$Ga_2O_3(\bar{2}01)$/AlN(0001) and ϵ/κ-Ga_2O_3(001)/AlN(0001) epilayers are of high crystalline quality. Growth and phase diagrams are developed to synthesize Ga_2O_3 on AlN by MBE and MOCATAXY and to provide guidance to grow Ga_2O_3 on several non-oxide surfaces, e.g., AlN, GaN, and SiC, by MBE, *S*-MBE, and MOCATAXY.

© *2023 Author(s). All article content, except where otherwise noted, is licensed under a Creative Commons Attribution (CC BY) license (http://creativecommons.org/licenses/by/4.0/).* https://doi.org/10.1063/5.0174373

14 November 2023 01:39:54

I. INTRODUCTION

Due to the increased demand for high-power and high-frequency applications to establish decentralized power plants and ultra-fast telecommunication,[1–3] there is growing interest in ultrawide bandgap (UWBG) materials with high electric field breakdown strengths. AlN, GaN, and SiC are established materials used in high-power metal-oxide-semiconductor field-effect transistors (MOSFETs) and high-electron-mobility transistors (HEMTs).[4–7]

Ga_2O_3 is an emerging UWBG semiconductor and has sparked tremendous interest as a novel material for high-power applications.[8,9] Monoclinic β-Ga_2O_3 is the most studied Ga_2O_3 polymorph, with an experimentally proven critical breakdown field strength larger than that of SiC and GaN.[10] Another UWBG polymorph is the metastable ϵ-Ga_2O_3 phase, which has recently attracted attention as it possesses strong spontaneous polarization,[11–14] potentially larger than that of GaN,[15,16] and potentially outperforming AlGaN/GaN or Si-modulation-doped β-Ga_2O_3/β-$(Al,Ga)_2O_3$ heterojunctions.[17,18] The crystal structure of ϵ-Ga_2O_3 is sometimes referred to as hexagonal ϵ-phase ($P6_3mc$) or orthorhombic κ-phase ($Pna2_1$).[19] For the sake of simplicity, we refer to this phase as ϵ-Ga_2O_3 in this work.

The fabrication of β-Ga_2O_3/AlN and ϵ-Ga_2O_3/AlN hybrids may be used to realize high-mobility, polarization-induced, two-dimensional electron gases (2DEGs) at their interfaces.[13,20] The growth of β-Ga_2O_3 and ϵ-Ga_2O_3 on AlN and GaN has been demonstrated by chemical vapor deposition (CVD) techniques,[11,21–26] and HEMTs using ϵ-Ga_2O_3/GaN[27] structures have been fabricated. No

© Author(s) 2023

studies of β-Ga_2O_3 or ϵ-Ga_2O_3 grown on AlN by MBE are reported in the literature.

The growth of Ga_2O_3 on oxide substrates by conventional MBE is limited by complex two-step kinetics and the desorption of its volatile suboxide Ga_2O.[28,29] To extend the kinetic and thermodynamic MBE parameter space under which Ga_2O_3 can be formed, two variants of MBE have been developed: (i) *suboxide* MBE (*S*-MBE)[30] and (ii) metal-oxide-catalyzed epitaxy (MOCATAXY).[31,32] *S*-MBE enables simple 1-step kinetics to form Ga_2O_3, allowing MBE growth rates to exceed 1 μm h^{-1} at lower growth temperatures (T_G).[33,34] *S*-MBE can use metal-oxide mixtures or solid compound sources to produce suboxides.[30,34–40] MOCATAXY results from metal-exchange catalysis (MEXCAT)[31,35,41] and refers to a growth process where elemental or molecular catalysts (e.g., In, Sn, In_2O, and SnO) and surface active agents (surfactants) are introduced to the growth system,[35] thereby increasing the yield of Ga_2O_3, $(Al_xGa_{1-x})_2O_3$, and In_2O_3, accompanied by improved crystalline and transport properties.[31,35,41–47]

In this paper, we demonstrate the growth of β-$Ga_2O_3(\bar{2}01)$ and ϵ-Ga_2O_3(001) on Al-polar AlN(0001). We use three different MBE approaches to explore the growth of Ga_2O_3 on AlN: (i) conventional MBE—hereafter referred to as "MBE"—, (ii) *S*-MBE, and (iii) MOCATAXY. These strategies allow us to investigate a wide parameter range of MBE growth conditions to form Ga_2O_3 films on III-N substrates. As a result, we obtain epilayers of β-Ga_2O_3 and ϵ-Ga_2O_3 on AlN with high crystalline quality and very smooth surface morphologies by *S*-MBE and MOCATAXY, respectively. To guide the nucleation, growth, and phase formation of Ga_2O_3 on AlN, we derive growth and phase diagrams for MBE and MOCATAXY.

II. EXPERIMENTAL SECTION

Ga_2O_3 films were grown by MBE and MOCATAXY in a plasma-assisted RIBER compact 12 system using atomic O as the reactive oxidant. The *S*-MBE grown Ga_2O_3 films were synthesized in a Veeco GEN10 MBE system using O_3 as the reactive oxidant. Ga (7N purity) and In (7N purity) were supplied from standard effusion cells during MBE and MOCATAXY growth. During *S*-MBE growth, Ga metal (7N purity) and Ga_2O_3 powder (5N purity) were used to produce molecular beams of Ga_2O from commercial dual-filament MBE effusion cells; see Ref. 30. Ga_2O_3 films were deposited on 1 μm thick, single-crystalline, Al-polar AlN(0001) non-vicinal template with rms roughnesses of rms ≈ 0.1 nm and full width half maxima (FWHM) of the 0002 peaks of FWHM ≈ 0.02°, epitaxially grown on Al_2O_3(0001) bulk substrates, purchased from DOWA Electronics Materials. For the *S*-MBE sample, in-house grown AlN templates were grown on Al_2O_3(0001) using optimized growth conditions in a Veeco GENxplor MBE system equipped with a standard effusion cell for Al and a radio frequency plasma source for active N species. These AlN templates have rms ≈ 0.4 nm and FWHM ≈ 0.03° of the 0002 peak of AlN(0001). The substrates were backside coated with an approximate 500 nm thick $Ti_{0.9}W_{0.1}$ alloy to ensure thermal radiation heating during growth. Before growth, AlN templates were cleaned *ex situ* and *in situ* by wet etching (piranha solution) and 2 min In-polishing, respectively, to eliminate surface contamination and unintentional surface oxidation. The growth temperature (T_G) was measured by a thermocouple located within the substrate heater and an optical pyrometer operating at a wavelength of 980 nm. During MBE and MOCATAXY growth, the O_2 flux (ϕ_{O_2}) was measured in standard cubic centimeters per min (SCCM), and radio-frequency plasma power of P_{rf} = 300 W was utilized to produce an active O molecular-beam, ϕ_O. Fluxes of Ga (ϕ_{Ga}) and In (ϕ_{In}) were measured as beam-equivalent pressures (BEPs) in mbar before growth with an ion gauge located at the growth position. The Ga_2O suboxide flux (ϕ_{Ga_2O}) was measured by a quartz crystal microbalance (QCM) in Å s^{-1} prior to growth. All fluxes were converted to growth rate units in nm min^{-1} and particle flux units in nm^{-2} s^{-1}, using film thickness data and the cation and anion densities in the respective polymorph, which were obtained under growth conditions when full cation and anion incorporation are guaranteed.[48] All growth parameters and conversions used in this work are summarized in Tables I and II.

To determine when thin film nucleation occurs and to identify phase formation, *in situ* reflection high-energy electron diffraction (RHEED) was utilized, using 14.5 keV electrons. X-ray reflectivity

14 November 2023 01:39:54

TABLE I. Sample numbers, MBE method, Ga_2O_3 phase, respective data symbols, and T_G for MBE, *S*-MBE, and MOCATAXY are provided, and values of ϕ_O, ϕ_{Ga}, ϕ_{Ga_2O}, and ϕ_{In} are given in nm^{-2} s^{-1}. The growth time (t) and film thickness (d) are collected as well.

Sample	Method	Phase	Symbol	T_G (°C)	ϕ_O	ϕ_{Ga}	ϕ_{Ga_2O}	ϕ_{In}	t (min)	d (nm)
I	MOCA.	ϵ-Ga_2O_3	◈	725	3.0	3.6	–	1.0	120	500
II	MOCA.	ϵ-Ga_2O_3	◇	700	3.0	3.6	–	1.0	15	45
III	MOCA.	ϵ-Ga_2O_3	○	700	3.0	3.6	–	0.5	35	107
IV	MOCA.	β-Ga_2O_3–ϵ-Ga_2O_3	⧫	625	3.0	3.6	–	1.0	20	74
V	MOCA.	β-Ga_2O_3–ϵ-Ga_2O_3	⊖	625	3.0	3.6	–	0.5	10	30
VI	MOCA.	amorp. β-Ga_2O_3	⊕	700	6.0	3.6	–	0.5	10	58
VII	MOCA.	β-Ga_2O_3	●	550	3.0	3.6	–	0.5	10	28
VIII	MOCA.	β-Ga_2O_3	⊙	550	3.0	1.8	–	0.9	42	100
IX	MBE	β-Ga_2O_3	□	550	3.0	0.8	–	–	15	20
X	*S*-MBE	β-Ga_2O_3	▲	525	0.7	–	1.7	–	40	40
XI	MBE	β-Ga_2O_3	■	550	3.0	3.6	–	–	15	20
XII	MBE	β-Ga_2O_3	◫	550	3.0	1.7	–	–	15	25
XIII	MBE	β-Ga_2O_3	⊡	700	2.0	0.8	–	–	53	44

© Author(s) 2023

(XRR) and optical reflectivity were employed to measure the film thicknesses of Ga_2O_3 *ex situ*. Longitudinal x-ray diffraction (XRD) (2θ-ω scans) and transverse XRD (ω-scans) were performed in a Philips X'Pert Pro MRD system (angular resolution ≈ 0.001°) with Cu $K\alpha_1$ radiation to identify phase formation and crystalline quality of the grown thin films. Atomic force microscopy (AFM) was employed to measure the surface morphologies and surface roughnesses in Ga_2O_3. To further study the crystallinity of the Ga_2O_3 films, micro-Raman (μ-Raman) spectroscopy was performed using a Kimmon HeCd laser with a wavelength of 442 nm and a LabRAM HR Evolution confocal spectrometer. For transmission electron microscopy (TEM), specimens were prepared by the focused ion beam (FIB) lift-out technique employing an FEI Nova 200 and a Kleindieck manipulator needle. The lamellas were then investigated in a ThermoFisher Spectra 300 equipped with the Super-X technology consisting of a high brightness field emission gun and a 4-quadrant energy dispersive x-ray detector. The current of the probe-corrected machine was adjusted using its monochromator unit to 20 pA for high resolution scanning TEM (HRSTEM).

III. GROWTH KINETICS AND GROWTH MODELS

Figure 1 provides growth-rate diagrams for β-$Ga_2O_3(\bar{2}01)$ and ϵ-$Ga_2O_3(001)$ formed on AlN(0001) by MBE, *S*-MBE, and MOCATAXY and shows the impact of accessible growth regimes on their respective growth rates, Γ. Model calculations taken from the literature for MBE (depicted as the blue areas),[29] *S*-MBE (depicted as the dashed area),[30] and MOCATAXY (depicted as the gray areas)[35] are used to provide *qualitative* guidance to the growth windows and regimes obtained for each MBE variant.

Figure 1(a) shows Γ obtained by MBE and MOCATAXY as a function of ϕ_{Ga}. In the O-rich regimes, Γ of β-Ga_2O_3 increases with ϕ_{Ga} until stoichiometric growth conditions are reached. In the Ga-rich regimes, Γ decreases with increasing ϕ_{Ga} due to Ga_2O desorption, and growth ceases in the vast excess of ϕ_{Ga}.[49] The MOCATAXY sample is grown under "effectively" more O-rich conditions as the catalyst In provides more O for Ga-to-Ga_2O_3 oxidation than is available for Ga in the absence of In.[31] The O-rich regime available by MOCATAXY is about 1.4 times wider than the O-rich regime accessed by MBE with $\Delta\phi_O = \phi'_O - \phi_O = (4.2 - 3.0)$ $nm^{-2}\,s^{-1} \approx 1.2\,nm^{-2}\,s^{-1}$ given in the figure. The O fluxes available for MOCATAXY and MBE are denoted as ϕ'_O and ϕ_O, respectively. Thus, Γ of β-Ga_2O_3 increases by $\Delta\Gamma \approx (2.8 - 1.3)$ nm min^{-1} = 1.5 nm min^{-1} at ϕ_{Ga} = 3.6 $nm^{-2}\,s^{-1}$ when using MOCATAXY. The MBE models shown here use the same kinetic parameters but different ϕ_O and ϕ'_O.

Figure 1(b) shows Γ of β-Ga_2O_3 grown by *S*-MBE as a function of ϕ_{Ga_2O}. In the O-rich regime, Γ increases with ϕ_{Ga_2O} until stoichiometric growth conditions are reached. In the Ga_2O-rich regime (i.e., in the adsorption-controlled regime), Γ is independent of ϕ_{Ga_2O} and reaches a plateau, with Γ being maximized. To

14 November 2023 01:39:54

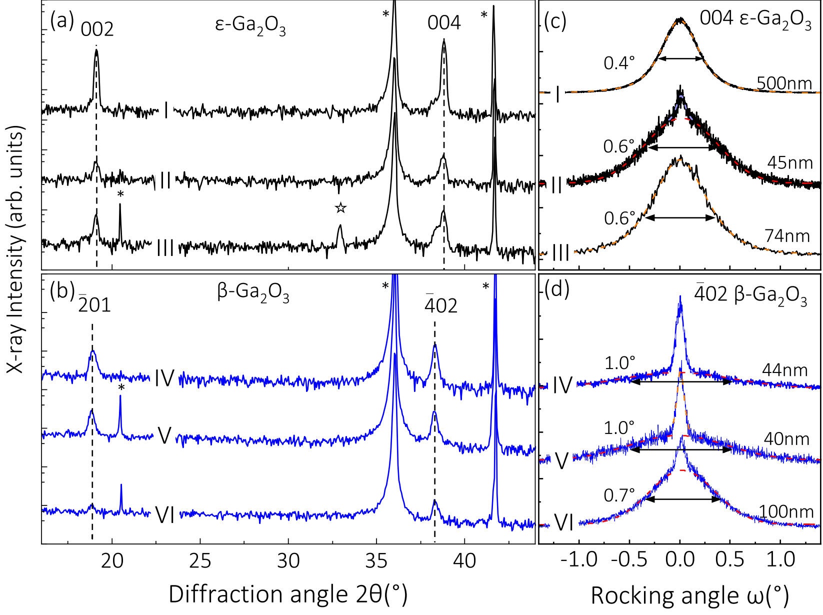

FIG. 1. Γ-diagrams of β-$Ga_2O_3(\bar{2}01)$ and ϵ-$Ga_2O_3(001)$ on AlN(0001). (a) Γ of β-$Ga_2O_3(\bar{2}01)$ as a function of ϕ_{Ga}. For MOCATAXY, ϕ_{In} = 0.5 $nm^{-2}\,s^{-1}$ was additionally supplied, resulting in a growth rate increase $\Delta\Gamma$ of β-$Ga_2O_3(\bar{2}01)$, as indicated in the figure. The expansion of the O-rich regime by MOCATAXY is indicated by $\Delta\phi_O$ at the corresponding stoichiometric points. (b) Γ of β-$Ga_2O_3(\bar{2}01)$ as a function of $\phi_{Ga_2O} = 1/2\phi_{Ga}$ by *S*-MBE and MBE.[30] The growth of Ga_2O_3 by *S*-MBE takes place in the adsorption-controlled regime with maximized Γ, whereas the growth of Ga_2O_3 by MBE is kinetically forbidden at the same $\phi_{Ga_2O} = 1/2\phi_{Ga}$, indicated by $\Delta\Gamma$ in the figure. (c) Γ of β-$Ga_2O_3(\bar{2}01)$ and ϵ-$Ga_2O_3(001)$ as a function of T_G by MBE and MOCATAXY. At ϕ_O = 3.0 $nm^{-2}\,s^{-1}$, the gray and gray-dashed areas in panel (c) refer to the regime where β-Ga_2O_3 and ϵ-Ga_2O_3 can be synthesized by MOCATAXY using an In-to-Ga flux ratio of $R = \phi_{In}/\phi_{Ga}$ = 0.5 and $R \approx 0.3$, respectively [see Fig. 7(b)]. All growth parameters and flux conversions are given in Tables I and II.

© Author(s) 2023

compare the growth domain accessed by S-MBE (the dashed area),[30] we model the growth domain accessed by MBE (the blue area).[29] This example illustrates that Ga_2O_3 formation can be kinetically forbidden by MBE in the adsorption-controlled regime (i.e., in the excess of ϕ_{Ga}). In contrast, Γ of Ga_2O_3 is maximized and independent of ϕ_{Ga_2O} by S-MBE in the adsorption-controlled regime (i.e., in the excess of ϕ_{Ga_2O}). With respect to Γ, the adsorption-controlled regime obtained for III-O materials by S-MBE[30,34] equals the adsorption-controlled regime obtained for III-N materials by MBE.[50–53]

Figure 1(c) shows Γ of β-Ga_2O_3 and ϵ-Ga_2O_3 grown by MBE and MOCATAXY as a function of T_G. At given T_G and ϕ_{In} used, Γ of β-Ga_2O_3 grown by MOCATAXY (the dotted disk) increases by $\Delta\Gamma \approx (2.4 - 1.3)$ nm min^{-1} = 1.1 nm min^{-1} compared with β-Ga_2O_3 grown by MBE (the solid square). Under growth conditions when Ga_2O_3 cannot be formed by MBE, the growth of ϵ-Ga_2O_3 becomes kinetically and thermodynamically stabilized by MOCATAXY, combined with high Γ plotted as the diamonds. Similar kinetics of Ga_2O_3 has been observed on different growth surfaces and polymorphs.[28,41,47,49]

IV. CRYSTAL PHASES AND SURFACE MORPHOLOGIES

We next discuss the influence of the different growth regimes shown in Fig. 1—i.e., the impact of ϕ_{Ga}, ϕ_{In}, ϕ_{Ga_2O}, ϕ_O, and T_G—on the crystalline structure, phase formation, and surface morphologies of Ga_2O_3/AlN.

Figures 2(a) and 2(b) show longitudinal XRD scans (2θ-ω scans) of selected ϵ-Ga_2O_3 and β-Ga_2O_3 films grown on AlN(0001), respectively. The reflections of the films coincide with those of the ϵ-Ga_2O_3 and β-Ga_2O_3 phases grown with their (001) plane and ($\bar{2}01$) plane, respectively, parallel to the (0001) plane of the AlN template. Based on the large lattice mismatch between β-Ga_2O_3 with AlN and ϵ-Ga_2O_3 with AlN,[18] we assume our Ga_2O_3 films are fully relaxed upon reaching a critical thickness of just a few nanometers. In the case of ϵ-Ga_2O_3 grown by MOCATAXY, we do not observe an increase in the c-plane lattice constant of ϵ-Ga_2O_3, i.e., no peak shift of 2θ to lower angles, indicating a negligible In incorporation into Ga_2O_3 of below 1%.

At low T_G and high metal fluxes (i.e., ϕ_{Ga} plus ϕ_{In}), we observe an additional diffraction peak at 2θ = 32.9° from metallic In,[55] as indicated by a star in Figs. 2(a) and 2(b) (samples IV and VII). The segregation and droplet formation of In when growing Ga_2O_3 by MOCATAXY at low T_G and high metal fluxes emerges due to the thermodynamic repulsion of In by Ga, since the Ga–O bonds are stronger than In–O bonds,[56] and because In may minimize the surface free energy of the growth system.[57] At low T_G and low ϕ_{In}, we observe the co-existence of the β-Ga_2O_3 and ϵ-Ga_2O_3 phases (samples IV and V). At high $T_G \geq 700\,°C$ and with longer growth times (t), the metastable ϵ-Ga_2O_3 may transform partially into β-Ga_2O_3 (see Fig. 6),[58] because of the thermal instability of ϵ-Ga_2O_3 at high T_G. For the used ϕ_O, the growth window where phase-pure ϵ-Ga_2O_3(001) on AlN(0001) can be achieved is relatively narrow; see Fig. 7(b).

Note that we identify that ϵ-Ga_2O_3 cannot be epitaxially stabilized by conventional MBE for the growth conditions explored. To verify this nature, we grew an ϵ-Ga_2O_3(001) nucleation layer on AlN(0001) with thickness $d \approx 10$ nm by MOCATAXY (same conditions as sample II) during a first growth step to exclude effects of Ga_2O_3 nucleation on AlN. By a second growth step, on top of the ϵ-Ga_2O_3(001) nucleation layer, we grew a $d \approx 24$ nm thick β-Ga_2O_3($\bar{2}01$) layer at T_G = 625 °C by MBE, as confirmed by XRD data (not shown). This experiment suggests that ϵ-Ga_2O_3 cannot be epitaxially stabilized on AlN by MBE.

To investigate and compare the crystalline quality of the β-Ga_2O_3 film with $d \approx 44$ nm (sample XIII) grown by MBE, the β-Ga_2O_3 film with $d \approx 40$ nm (sample X) grown by S-MBE, and the ϵ-Ga_2O_3 film with $d \approx 45$ nm grown by MOCATAXY (sample II), Figs. 3(a) and 3(b) show transverse XRD scans (ω-scans) of the $\bar{4}02$ peaks of β-Ga_2O_3 and 004 peaks of ϵ-Ga_2O_3 in symmetric geometry, respectively. Figures 3(c) and 3(d) show corresponding μ-Raman spectra taken for the same β-Ga_2O_3 films as plotted in

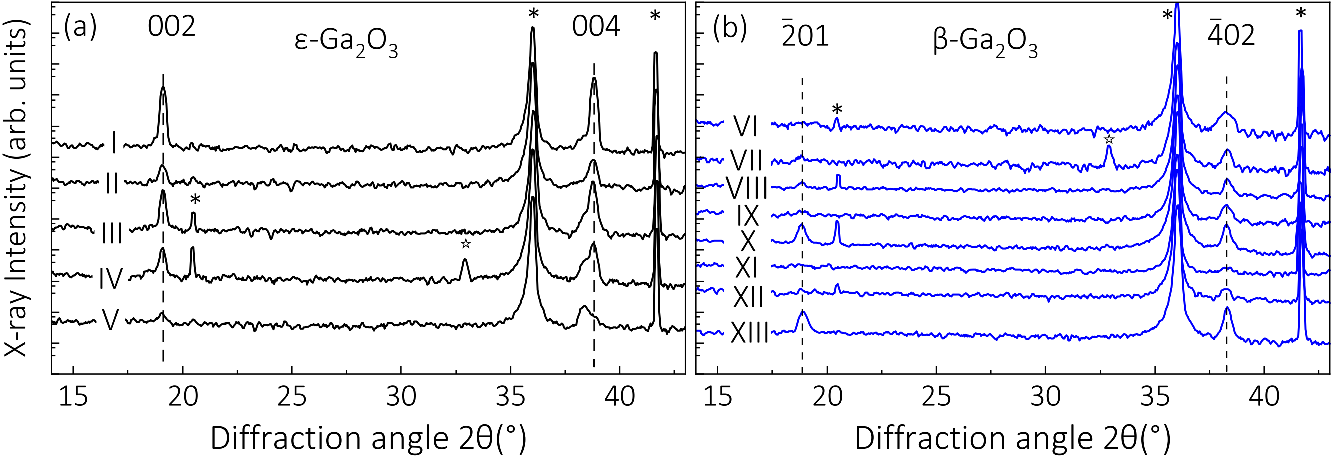

FIG. 2. Longitudinal XRD scans recorded for (a) ϵ-Ga_2O_3 and (b) β-Ga_2O_3 grown on AlN(0001)/Al_2O_3(0001) templates by MBE, S-MBE, and MOCATAXY. The reflections from the Ga_2O_3 films originate either from the ϵ-phase[19] or the β-phase.[54] The peaks of the AlN and Al_2O_3 substrates are marked by asterisks. Table I collects all the growth parameters of the samples plotted here.

14 November 2023 01:39:54

© Author(s) 2023

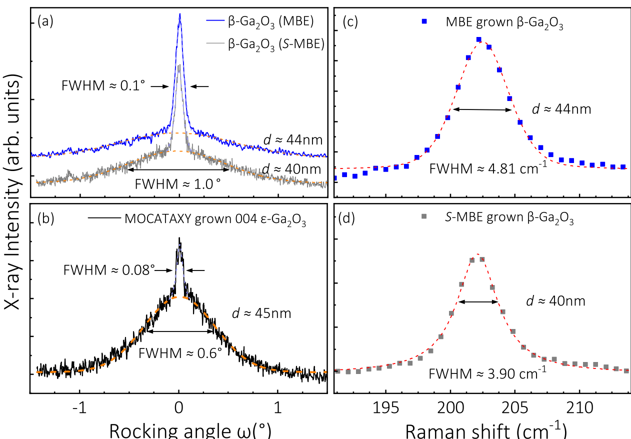

FIG. 3. (a) Transverse XRD scans of the $\bar{4}02$ peak of β-Ga_2O_3 grown by MBE (sample XIII) and *S*-MBE (sample X). Both films possess the same FWHM, as indicated in the figure. (b) Transverse XRD scan of the 004 peak of ϵ-Ga_2O_3 grown by MOCATAXY (sample II). (c) and (d) μ-Raman spectra of the same β-Ga_2O_3 films plotted in panel (a) showing the $A_g^{(3)}$ Raman mode of β-Ga_2O_3 obtained for MBE and *S*-MBE, respectively. Γ and surface morphologies of the same samples are shown in Figs. 1 and 4. XRD data were fit by Gaussian functions (the broad peak) and Lorentzian functions (the narrow peak). Raman data were fitted by Voigt functions. All FWHM have been extracted by corresponding data fits and functions. Film thicknesses (d) are indicated in the figures.

Fig. 3(a). We tried to measure a μ-Raman spectrum for our ϵ-Ga_2O_3 film with $d \approx 500$ nm but have not detected a Raman mode for this film. This lets us conclude that the Raman modes for ϵ-Ga_2O_3 are marginally active. This observation is in accordance with Ref. 41. Here, the authors measured a ϵ-Ga_2O_3 film with $d \approx 1130$ nm by Raman spectroscopy in confocal mode and observed very weak Raman signals from this "thick" ϵ-Ga_2O_3 film.[41]

We extract the full width at half maxima (FWHM) obtained by transverse XRD scans (ω-scans) of selected β-Ga_2O_3 [Fig. 3(a)] and ϵ-Ga_2O_3 films [Fig. 3(b)]. This FWHM is a measure for the out-of-plane mosaic spread, twisting of crystallites, and defect densities in epitaxial thin films.[26,59] As theoretically calculated,[60,61] the observed 2-component XRD transverse scans of the β-Ga_2O_3 and ϵ-Ga_2O_3 films may originate from uncorrelated dislocations (the broad peak) and correlated dislocations (the narrow peak); similar 2-component transverse scans have been observed in other material systems.[62–65] The FWHM obtained for the $A_g^{(3)}$ Raman mode for β-Ga_2O_3 grown by MBE and *S*-MBE is also indicated in Figs. 3(c) and 3(d). The FWHM obtained by μ-Raman spectra also indicates the defect density and crystallinity quality of thin films.[66] In other words, the narrower the FWHM obtained by ω-scans and μ-Raman spectra, the lower the defect density and the higher the crystallinity of the respective epitaxial film.

According to these XRD and μ-Raman spectra results, we conclude that phase-pure β-Ga_2O_3 and phase-pure ϵ-Ga_2O_3 films on AlN(0001) can be realized by MBE (sample XIII), *S*-MBE (sample X), and MOCATAXY (sample II) at a high crystalline level, with negligible In incorporation in the case of MOCATAXY-grown films.

Figure 4 depicts the surface morphologies of the same samples plotted in Fig. 2, measured by AFM. It shows the influence of

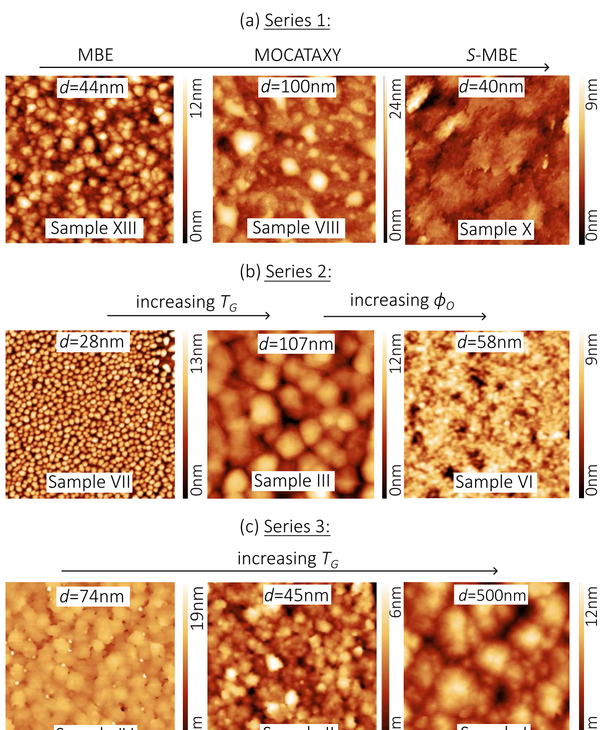

FIG. 4. (a)–(c) Surface morphologies obtained from 1×1 μm^2 AFM scans for ϵ-Ga_2O_3 and β-Ga_2O_3 surfaces plotted as series 1, series 2, and series 3. The obtained root mean square (rms) roughnesses are plotted in Fig. 5. The growth parameters are provided in Table I, and sample numbers and film thicknesses (d) are indicated in the figures.

different growth parameters and MBE variants on the topography of β-Ga_2O_3 and ϵ-Ga_2O_3 deposited on AlN. In series 1 [Figs. 4(a) and 5(a)], the influence of different MBE variants (MBE, MOCATAXY, and *S*-MBE) on the surface morphology of β-$Ga_2O_3(\bar{2}01)$ is shown. For the growth conditions employed, *S*-MBE minimizes the surface roughness for β-$Ga_2O_3(\bar{2}01)$/AlN(0001) (sample X). We stress that more *S*-MBE films need to be grown to solidify this observation.

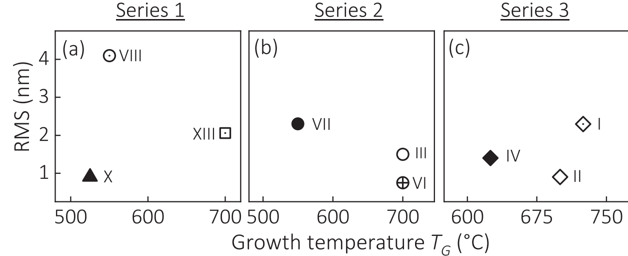

FIG. 5. (a)–(c) Root mean square (rms) roughness as a function of T_G for Ga_2O_3 grown by MBE, *S*-MBE, and MOCATAXY. The symbols shown here correspond to the same samples and symbols shown in Fig. 1. The different series indicated on top of the figures are the same as shown in Fig. 4.

14 November 2023 01:39:54

© Author(s) 2023

In series 2 [Figs. 4(b) and 5(b)], the influence of T_G and ϕ_O on the morphology of Ga_2O_3 grown by MOCATAXY is shown. At low T_G, phase-pure β-Ga_2O_3 with In droplets formed on the growth surface is observed (sample VII), roughening the film surface. Increasing T_G results in a phase-jump from β-Ga_2O_3 to almost phase-pure ϵ-Ga_2O_3, with overall improved surface morphology and increased grain sizes (sample III). At the same T_G, once ϕ_O is increased, the crystalline structure of ϵ-Ga_2O_3 collapses, and a mixture of amorphous Ga_2O_3 and β-Ga_2O_3 is detected (Sample VI). That MOCATAXY becomes less effective (or even suppressed) under O-rich conditions can be explained by the higher O surface densities and reduced catalytic activity in these growth regimes.[48]

In series 3 [Figs. 4(c) and 5(c)], the effect of T_G on the surface structure of ϵ-Ga_2O_3 is studied. With increasing T_G, the rms roughness shows a minimum at intermediate T_G. This feature may be explained by the enhanced surface diffusion of In combined with an enhanced In desorption (reduced surface lifetime) at higher T_G. These competing surface effects might explain our minimized rms values obtained at intermediate T_G and are a common feature in MBE, e.g., as observed for homoepitaxially grown β-Ga_2O_3(010) by MBE.[67] Note that we also measured the surface morphology of sample IV without including In droplets and obtained a similar rms value as plotted in Fig. 5(c), for which the In droplets were included in calculating the surface roughness.

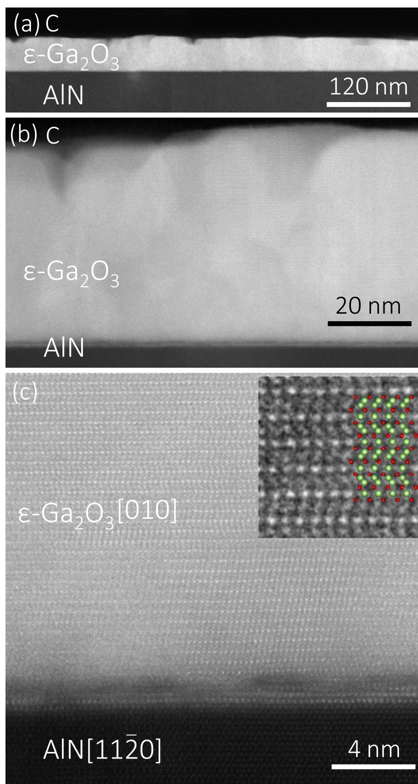

FIG. 6. STEM images of ϵ-Ga_2O_3(001)/AlN(0001) (sample II) grown by MOCATAXY. (a) Overall surface morphology of the ϵ-Ga_2O_3(001)/AlN(0001) heterostructure with carbon (C) coating on top of the ϵ-Ga_2O_3 film. (b) High-resolution STEM (HRSTEM) image of the same ϵ-Ga_2O_3 film. (c) HRSTEM image along the 11$\bar{2}$0 zone axes of AlN and the [010] zone axes of ϵ-Ga_2O_3. Inset: Crystallographic model of the ϵ-Ga_2O_3[010] rotation domain showing the atomic structure of ϵ-Ga_2O_3. Ga and O atoms are displayed in green and red, respectively. Discussion in the text.

V. ATOMIC STRUCTURE OF ϵ-GA_2O_3/AlN

To reveal the atomic structure and crystallinity of a selected ϵ-Ga_2O_3/AlN sample, Fig. 6 shows the STEM images of ϵ-Ga_2O_3(001) (sample II) taken along the [11$\bar{2}$0] zone axis of the AlN template. Figure 6(a) depicts an overview of the epilayer, showing a uniform and crystalline ϵ-Ga_2O_3(001) film. Figure 6(b) shows a more detailed overview of the ϵ-Ga_2O_3 film. Defects such as dislocations are not observed in this layer or the measured sample area. The slight density contrast emerges from the three different rotation domains existing in ϵ-Ga_2O_3(001)/AlN(0001).[68,69] Figure 6(c) shows a high-resolution STEM image of this ϵ-Ga_2O_3(001)/AlN(0001) heterostructure. After a 2-monolayer thick nucleation layer, we detect a "darker" intensity contrast, suggesting the onset of a ϵ-Ga_2O_3 → β-Ga_2O_3 phase transition at the ϵ-Ga_2O_3-AlN heterointerface. This idea is supported by other studies showing that ϵ-Ga_2O_3 potentially transforms into β-Ga_2O_3 for $T_G \geq 700\,^\circ$C.[58] We thus conclude that during the initial growth phase, ϵ-Ga_2O_3 forms and nucleates on AlN and grows as ϵ-Ga_2O_3 thin film. After a given growth time and used $T_G = 700\,^\circ$C, this meta-stable ϵ-Ga_2O_3 might gradually transform to the more stable β-Ga_2O_3 phase at the Ga_2O_3-AlN interface. We stress, however, that further studies are required to understand this interface property and are beyond the scope of this work. In addition, the inset in Fig. 6(c) displays a crystallographic model of the ϵ-Ga_2O_3[010] rotation domain of the ϵ-Ga_2O_3(001) epilayer, showing a highly ordered atomic structure of this ϵ-Ga_2O_3(001) film.

VI. GROWTH AND PHASE DIAGRAM

To provide guidance for the epitaxial growth of β-Ga_2O_3/AlN and ϵ-Ga_2O_3/AlN by MBE and MOCATAXY, we derive a growth diagram for MBE as well as a growth and phase diagram for MOCATAXY. These are depicted in Figs. 7(a) and 7(b), respectively.

Figure 7(a) shows the fundamental nucleation and growth window of β-Ga_2O_3($\bar{2}$01) on AlN(0001) obtained by MBE. The regime where no nucleation of Ga_2O_3 on AlN(0001) occurs is marked by the white area. The solid line shows the model calculation and interface where Γ of Ga_2O_3 on AlN(0001) becomes larger than zero, i.e., $\Gamma > 0$. The decrease in the maximum possible r with T_G (the solid line) results from reduced Ga and O sticking at higher T_G and is extracted from the model on Al_2O_3(0001) given in Ref. 48, which also very accurately models our experimental data obtained on AlN(0001). The growth diagram is divided into two regimes. Regime (i) consists of crystalline Ga_2O_3 films exhibiting relatively smooth surfaces identified by streaky RHEED patterns (data not shown), and regime (ii) has relatively rough surfaces identified by spotty RHEED patterns (data not shown). Furthermore, the crystalline quality of β-Ga_2O_3 grown by MBE decreases with increasing ϕ_{Ga} (as indicated in Fig. 2).

Figure 7(b) displays the phase diagram and growth window of Ga_2O_3 on AlN(0001) obtained by MOCATAXY. We divide this

14 November 2023 01:39:54

© Author(s) 2023

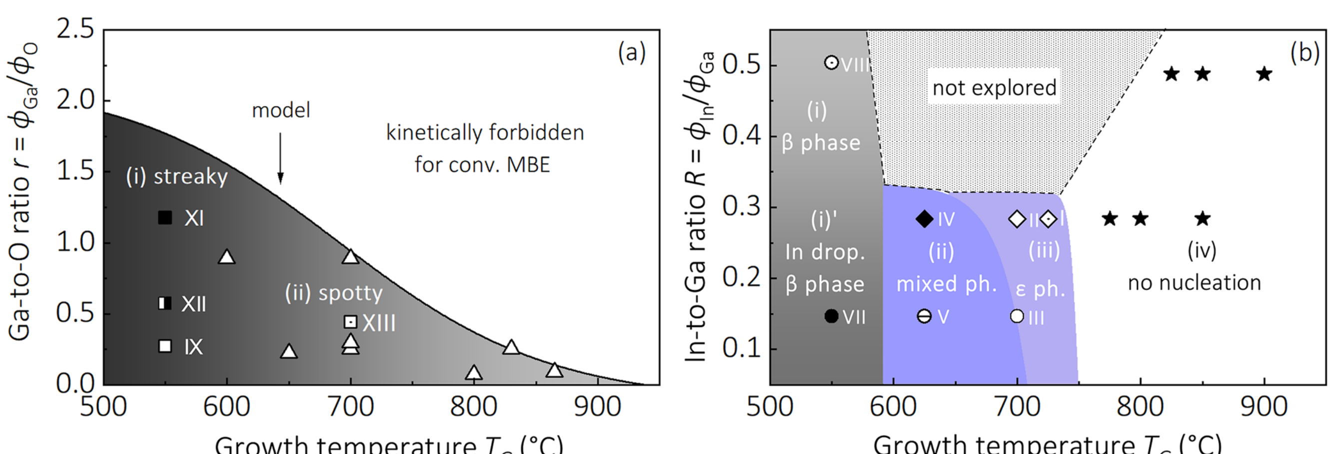

FIG. 7. (a) Growth window under which β-Ga_2O_3 nucleation and growth are feasible on AlN(0001), projected onto the two-dimensional parameter space spanned by the Ga-to-O flux ratio (r) and growth temperature (T_G). Samples plotted as squares are shown in Fig. 1. Samples plotted as open triangles are crystalline β-$Ga_2O_3(\bar{2}01)$ films with $\Gamma > 0$ (not shown elsewhere in this work). (b) Phase diagram for Ga_2O_3 on AlN(0001) obtained by MOCATAXY, projected onto the 2-dimensional parameter space spanned by the In-to-Ga flux ratio (R) and T_G at fixed ϕ_O = 3.0 nm^{-2} s^{-1}. Sample numbers and symbols are indicated and correspond to those also used in Figs. 1, 2, and 4. The scale in panel (b) starts from $R \geq 0.05$. As for $R < 0.05$, we anticipate no or only a weak catalytic effect of In on Ga_2O_3 under the given growth conditions. As a first approach, the interfaces for each regime are obtained by an iterative approach using our available experimental data.

phase diagram into four major regimes. Regime (i) consists of phase-pure β-$Ga_2O_3(\bar{2}01)$ with relatively smooth surfaces and increased Γ. Regime (i)′ is similar to regime (i) but with In droplets formed on top of the β-$Ga_2O_3(\bar{2}01)$ surface. Note that sample VII is grown under more metal-rich conditions than sample VIII, i.e., using twice as much ϕ_{Ga}. Regime (ii) displays the regime where co-existing β-Ga_2O_3–ϵ-Ga_2O_3 is formed. Regime (iii) reflects the parameter space under which phase-pure ϵ-Ga_2O_3(001) is obtained and is relatively narrow for the ϕ_O used. Regime (iv) illustrates the regime where no nucleation and growth of Ga_2O_3 occurs on AlN(0001) for the supplied ϕ_O. The dotted area indicates the growth parameter space we have not yet explored.

VII. CONCLUSIONS

The growth of phase-pure β-$Ga_2O_3(\bar{2}01)$ and phase-pure ϵ-Ga_2O_3(001) on AlN(0001) by MBE, *S*-MBE, and MOCATAXY is demonstrated. Growth and phase diagrams for Ga_2O_3 grown by MBE and MOCATAXY are derived, depending on ϕ_{Ga}, ϕ_O, ϕ_{In}, and T_G, and show the influence of growth conditions on the crystalline properties and surface morphologies of Ga_2O_3. The concept of metal-exchange catalysis (MEXCAT)[31] is extended from III-O materials to III-N materials and to grow ϵ-Ga_2O_3(001)/AlN(0001) heterostructures by MOCATAXY. In addition, the concept of suboxide-mediated growth of oxide thin films is expanded from oxide surfaces to nitride surfaces, i.e., to grow β-$Ga_2O_3(\bar{2}01)$/AlN(0001) by *S*-MBE. STEM data of a selected ϵ-Ga_2O_3(001)/AlN(0001) heterostructure show an atomically ordered ϵ-Ga_2O_3 thin film with no extended defects such as dislocations observed within this layer.

Our findings provide guidance for the growth of β-Ga_2O_3 and ϵ-Ga_2O_3 on AlN and other non-oxide substrates, such as GaN and SiC. Our results open the door to realizing polarization-induced two-dimensional electron gases in Ga_2O_3/AlN, Ga_2O_3/GaN, and Ga_2O_3/SiC heterostructures.[13]

ACKNOWLEDGMENTS

M. A.-O. acknowledges the financial support from the Central Research Development Fund (CRDF) of the University of Bremen. J.P.M. acknowledges the support of a National Science Foundation Graduate Research Fellowship under Grant No. DGE2139899 and acknowledges the generous support through the German Academic Exchange Service scholarship.

AUTHOR DECLARATIONS

Conflict of Interest

The authors P.V. and D.G.S. have been granted U.S. Patent No. 11,462,402 (4 October 2022) with the title "Suboxide Molecular-Beam Epitaxy and Related Structures."

Author Contributions

Sushma Raghuvansy: Conceptualization (equal); Data curation (lead); Formal analysis (lead); Investigation (lead); Methodology (equal); Writing – original draft (lead); Writing – review & editing (lead). **Jon P. McCandless**: Conceptualization (equal); Formal analysis (equal); Investigation (lead); Methodology (equal); Writing – review & editing (supporting). **Marco Schowalter**: Formal analysis (supporting); Methodology (supporting); Writing – review & editing (supporting). **Alexander Karg**: Investigation (supporting); Methodology (supporting); Writing – review & editing (supporting). **Manuel Alonso-Orts**: Investigation (supporting);

14 November 2023 01:39:54

© Author(s) 2023

TABLE II. Collected flux conversions of ϕ_{Ga}, ϕ_{In}, ϕ_{Ga_2O}, and ϕ_O, for samples grown by MBE, S-MBE, and MOCATAXY. More growth parameters are provided in Table I. The active O flux for MBE and MOCATAXY samples is $\phi_O = 3.0\ nm^{-2}\ s^{-1}$, supplied from $\phi_{O_2} = 0.25$ SCCM and $P_{rf} = 300$ W. Conversions for the S-MBE grown samples are taken from Ref. 30.

Unit	ϕ_{Ga}	ϕ_{In}	ϕ_{Ga_2O}	ϕ_O (MBE)	ϕ_O (S-MBE)
10^{-7} mbar	1.0	1.0	⋯	⋯	13.3
nm min^{-1}	1.13	0.72	6.0	2.1	1.1
Å s^{-1}	0.19	0.12	1.0	0.35	0.18
$nm^{-2}\ s^{-1}$	0.76	0.37	2.3	3.0	0.70

Writing – review & editing (supporting). **Martin S. Williams**: Formal analysis (supporting); Writing – review & editing (supporting). **Christian Tessarek**: Investigation (supporting); Writing – review & editing (supporting). **Stephan Figge**: Formal analysis (supporting); Writing – review & editing (supporting). **Kazuki Nomoto**: Resources (supporting). **Huili Grace Xing**: Conceptualization (supporting); Resources (supporting). **Darrell G. Schlom**: Funding acquisition (supporting); Methodology (supporting); Resources (supporting). **Andreas Rosenauer**: Funding acquisition (supporting); Writing – review & editing (supporting). **Debdeep Jena**: Conceptualization (lead); Formal analysis (supporting); Funding acquisition (equal); Methodology (equal); Resources (equal); Writing – review & editing (supporting). **Martin Eickhoff**: Formal analysis (supporting); Funding acquisition (lead); Resources (lead); Supervision (equal); Writing – review & editing (supporting). **Patrick Vogt**: Conceptualization (lead); Formal analysis (equal); Investigation (lead); Methodology (lead); Project administration (lead); Supervision (lead); Writing – original draft (equal); Writing – review & editing (lead).

DATA AVAILABILITY

The data that support the findings of this study are available from the corresponding author upon reasonable request.

APPENDIX: FLUX CONVERSIONS

Table II collects the flux conversions of ϕ_{Ga}, ϕ_{In}, ϕ_{Ga_2O}, and ϕ_O, for samples grown by MBE, S-MBE, and MOCATAXY plotted in Figs. 1, 2, and 7.

REFERENCES

[1] L. F. S. Alves, R. C. M. Gomes, P. Lefranc, R. D. A. Pegado, O. P. Jeannin, B. A. Luciano, and F. V. Rocha, in *Brazilian Power Electronics Conference (COBEP)*, Juiz de Fora, Brazil, 2017 (IEEE, Piscataway, NJ, 2017), pp. 1–8.

[2] D. Pan, in *5th International Conference on Green Energy and Applications (ICGEA)*, Singapore, 2021 (IEEE, Piscataway, NJ, 2021), pp. 38–41.

[3] S. K. Mazumder, A. Kulkarni, S. Sahoo, F. Blaabjerg, H. A. Mantooth, J. C. Balda, Y. Zhao, J. A. Ramos-Ruiz, P. N. Enjeti, P. R. Kumar, L. Xie, J. H. Enslin, B. Ozpineci, A. Annaswamy, H. L. Ginn, F. Qiu, J. Liu, B. Smida, C. Ogilvie, J. Ospina, C. Konstantinou, M. Stanovich, K. Schoder, M. Steurer, T. Vu, and L. He, E. P. de la Fuente, IEEE J. Emerging Sel. Top. Power Electron. **9**, 5146–5163 (2021).

[4] J. W. Palmour, in *IEEE International Electron Devices Meeting* (IEEE, San Francisco, CA, 2014), pp. 1.1.1–1.1.8.

[5] U. Mishra, P. Parikh, and Y. F. Wu, Proc. IEEE **90**, 1022–1031 (2002).

[6] N. Herbecq, I. Roch-Jeune, A. Linge, B. Grimbert, M. Zegaoui, and F. Medjdoub, Electron. Lett. **51**, 1532–1534 (2015).

[7] J. Singhal, R. Chaudhuri, A. Hickman, V. Protasenko, H. G. Xing, and D. Jena, APL Mater. **10**, 111120 (2022).

[8] M. Higashiwaki, AAPPS Bull. **32**, 3 (2022).

[9] A. J. Green, J. Speck, G. Xing, P. Moens, F. Allerstam, K. Gumaelius, T. Neyer, A. Arias-Purdue, V. Mehrotra, A. Kuramata, K. Sasaki, S. Watanabe, K. Koshi, J. Blevins, O. Bierwagen, S. Krishnamoorthy, K. Leedy, A. R. Arehart, A. T. Neal, S. Mou, S. A. Ringel, A. Kumar, A. Sharma, U. Ghosh, K. Singisetti, W. Li, K. Chabak, K. Liddy, A. Islam, S. Rajan, S. Graham, S. Choi, Z. Cheng, and M. Higashiwaki, APL Mater. **10**, 029201 (2022).

[10] A. J. Green, K. D. Chabak, E. R. Heller, R. C. Fitch, M. Baldini, A. Fiedler, K. Irmscher, G. Wagner, Z. Galazka, S. E. Tetlak, A. Crespo, K. Leedy, and G. H. Jessen, IEEE Electron Device Lett. **37**, 902–905 (2016).

[11] F. Mezzadri, G. Calestani, F. Boschi, D. Delmonte, M. Bosi, and R. Fornari, Inorg. Chem. **55**, 12079 (2016).

[12] M. B. Maccioni and V. Fiorentini, Appl. Phys. Express **9**, 041102 (2016).

[13] J. L. Lyons, ECS J. Solid State Sci. Technol. **8**, Q3226 (2019).

[14] J. Kim, D. Tahara, Y. Miura, and B. G. Kim, Appl. Phys. Express **11**, 061101 (2018).

[15] F. Bernardini, V. Fiorentini, and D. Vanderbilt, Phys. Rev. B **56**(16), R10024 (1997).

[16] O. Ambacher, B. Foutz, J. Smart, J. R. Shealy, N. G. Weimann, K. Chu, M. Murphy, A. J. Sierakowski, W. J. Schaff, L. F. Eastman, R. Dimitrov, A. Mitchell, and M. Stutzmann, J. Appl. Phys. **87**, 334–344 (2000).

[17] S. Krishnamoorthy, Z. Xia, S. Bajaj, M. Brenner, and S. Rajan, Appl. Phys. Express **10**, 051102 (2017).

[18] S. B. Cho and R. Mishra, Appl. Phys. Lett. **112**, 162101 (2018).

[19] I. Cora, F. Mezzadri, F. Boschi, M. Bosi, M. Ćaplovićová, G. Calestani, I. Dódony, B. Pécz, and R. Fornari, CrystEngComm **19**, 1509–1516 (2017).

[20] A. F. M. A. U. Bhuiyan, Z. Feng, H. Huang, L. Meng, J. Hwang, and H. Zhao, J. Vac. Sci. Technol. A **40**, 062704 (2022).

[21] A. Polyakov, V. I. Nikolaev, A. I. Pechnikov, E. Yakimov, S. Y. Karpov, S. I. Stepanov, I. V. Shchemerov, A. A. Vasilev, A. V. Chernykh, A. Kuznetsov, I. H. Lee, and S. J. Pearton, J. Alloys Compd. **936**, 168315 (2023).

[22] Y. Ogura, Y. Arata, H. Nishinaka, and M. Yoshimoto, Jpn. J. Appl. Phys. **61**, SC1037 (2022).

[23] Y. Li, Y. Zhang, J. Zhang, T. Zhang, S. Xu, L. Feng, Q. Feng, C. Zhang, and Y. Hao, Semicond. Sci. Technol. **37**, 095004 (2022).

[24] S. Leone, R. Fornari, M. Bosi, V. Montedoro, L. Kirste, P. Doering, F. Benkhelifa, M. Prescher, C. Manz, V. Polyakov, and O. Ambacher, J. Cryst. Growth **534**, 125511 (2020).

[25] D. Tahara, H. Nishinaka, S. Morimoto, and M. Yoshimoto, Jpn. J. Appl. Phys. **56**, 078004 (2017).

[26] Y. Oshima, E. G. Víllora, Y. Matsushita, S. Yamamoto, and K. Shimamura, J. Appl. Phys. **118**, 085301 (2015).

[27] H. Y. Kang, M. J. Yeom, J. Y. Yang, Y. Choi, J. Lee, C. Park, G. Yoo, and R. B. Kyu Chung, Mater. Today Phys. **31**, 101002 (2023).

[28] M.-Y. Tsai, O. Bierwagen, M. E. White, and J. S. Speck, J. Vac. Sci. Technol., A **28**, 354–359 (2010).

[29] P. Vogt and O. Bierwagen, Phys. Rev. Mater. **2**, 120401 (2018).

[30] P. Vogt, F. V. E. Hensling, K. Azizie, C. S. Chang, D. Turner, J. Park, J. P. McCandless, H. Paik, B. J. Bocklund, G. Hoffman, O. Bierwagen, D. Jena, H. G. Xing, S. Mou, D. A. Muller, S. L. Shang, Z. K. Liu, and D. Schlom, APL Mater. **9**, 031101 (2021).

[31] P. Vogt, O. Brandt, H. Riechert, J. Lähnemann, and O. Bierwagen, Phys. Rev. Lett. **119**, 196001 (2017).

14 November 2023 01:39:54

© Author(s) 2023

[32]P. Vogt, A. Mauze, F. Wu, B. Bonef, and J. S. Speck, Appl. Phys. Express **11**, 115503 (2018).
[33]P. Vogt, D. G. Schlom, F. V. E. Hensling, K. Azizie, Z.-K. Liu, B. J. Bocklund, and S.-L. Shang, U.S. patent 11462402B2 (4 October 2022).
[34]K. Azizie, F. V. E. Hensling, C. A. Gorsak, Y. Kim, N. A. Pieczulewski, D. M. Dryden, M. K. I. Senevirathna, S. Coye, S. L. Shang, J. Steele, P. Vogt, N. A. Parker, Y. A. Birkhölzer, J. P. McCandless, D. Jena, H. G. Xing, Z. K. Liu, M. D. Williams, A. J. Green, K. Chabak, D. A. Muller, A. T. Neal, S. Mou, M. O. Thompson, H. P. Nair, and D. G. Schlom, APL Mater. **11**, 041102 (2023).
[35]P. Vogt, F. V. E. Hensling, K. Azizie, J. McCandless, J. Park, K. DeLello, D. A. Muller, H. G. Xing, D. Jena, and D. Schlom, Phys. Rev. Appl. **17**, 034021 (2022).
[36]F. V. E. Hensling, M. A. Smeaton, V. Show, K. Azizie, M. R. Barone, L. Kourkoutis, and D. G. Schlom, J. Vac. Sci. Technol., A **40**, 062707 (2022).
[37]A. B. Mei, L. Miao, M. J. Wahila, G. Khalsa, Z. Wang, M. Barone, N. J. Schreiber, L. E. Noskin, H. Paik, T. E. Tiwald, Q. Zheng, R. T. Haasch, D. G. Sangiovanni, L. F. J. Piper, and D. G. Schlom, Phys. Rev. Mater. **3**, 105202 (2019).
[38]K. M. Adkison, S.-L. Shang, B. J. Bocklund, D. Klimm, D. G. Schlom, and Z.-K. Liu, APL Mater. **8**, 081110 (2020).
[39]G. Hoffmann, M. Budde, P. Mazzolini, and O. Bierwagen, APL Mater. **8**, 031110 (2020).
[40]T. Kuznetsova, J. Roth, J. Lapano, A. Pogrebnyakov, and R. Engel-Herbert, J. Vac. Sci. Technol. A **41**, 053412 (2023).
[41]M. Kracht, A. Karg, J. Schörmann, M. Weinhold, D. Zink, F. Michel, M. Rohnke, M. Schowalter, B. Gerken, A. Rosenauer, P. J. Klar, J. Janek, and M. Eickhoff, Phys. Rev. Appl. **8**, 054002 (2017).
[42]P. Mazzolini, P. Vogt, R. Schewski, C. Wouters, M. Albrecht, and O. Bierwagen, APL Mater. **7**, 022511 (2019).
[43]A. Mauze, Y. Zhang, T. Itoh, F. Wu, and J. S. Speck, APL Mater. **8**, 021104 (2020).
[44]P. Mazzolini, A. Falkenstein, C. Wouters, R. Schewski, T. Markurt, Z. Galazka, M. Martin, M. Albrecht, and O. Bierwagen, APL Mater. **8**, 011107 (2020).
[45]A. Mauze, Y. Zhang, T. Itoh, E. Ahmadi, and J. S. Speck, APL Mater. **117**, 222102 (2020).
[46]T. Itoh, A. Mauze, Y. Zhang, and J. S. Speck, APL Mater. **11**, 041108 (2023).
[47]J. P. McCandless, D. Rowe, N. Pieczulewski, V. Protasenko, M. Alonso-Orts, M. S. Williams, M. Eickhoff, H. G. Xing, D. A. Muller, D. Jena, and P. Vogt, Jpn. J. Appl. Phys. **62**, SF1013 (2023).
[48]P. Vogt, "Growth kinetics, thermodynamics, and phase formation of group-III and IV oxides during molecular beam epitaxy," Ph.D. thesis, Humboldt University of Berlin, 2017.
[49]P. Vogt and O. Bierwagen, Appl. Phys. Lett. **108**, 072101 (2016).
[50]S. Fernández-Garrido, G. Koblmüller, E. Calleja, and J. S. Speck, J. Appl. Phys. **104**, 033541 (2008).
[51]S. Fernández-Garrido, Ź. Gaćeviá, and E. Calleja, Appl. Phys. Lett. **93**, 191907 (2008).
[52]E. Calleja, M. Sánchez-Garcıa, F. J. Sánchez, F. Calle, F. B. Naranjo, E. Muñoz, S. I. Molina, A. M. Sánchez, F. J. Pacheco, and R. Garcıa, J. Cryst. Growth **201-202**, 296 (1999).
[53]H. Riechert, R. Averbeck, A. Graber, M. Schienle, U. Strauβ, and H. Tews, MRS Proc. **449**, 149–159 (1996).
[54]J. Ahman, G. Svensson, and J. Albertsson, Acta Crystallogr., Sect. C: Cryst. Struct. Commun. **52**, 1336–1338 (1996).
[55]C. Tessarek, S. Fladischer, C. Dieker, G. Sarau, B. Hoffmann, M. Bashouti, M. Göbelt, M. Heilmann, M. Latzel, E. Butzen, S. Figge, A. Gust, K. Höflich, T. Feichtner, M. Büchele, K. Schwarzburg, E. Spiecker, and S. Christiansen, Nano Lett. **16**, 3415–3425 (2016).
[56]P. Vogt and O. Bierwagen, APL Mater. **4**, 086112 (2016).
[57]J. Neugebauer, Physica Status Solidi C **0**, 1651–1667 (2003).
[58]M. Bosi, L. Seravalli, P. Mazzolini, F. Mezzadri, and R. Fornari, Cryst. Growth Des. **21**, 6393–6401 (2021).
[59]V. M. Kaganer, R. Köhler, M. Schmidbauer, R. Opitz, and B. Jenichen, Phys. Rev. B **55**, 1793 (1997).
[60]V. M. Kaganer, O. Brandt, A. Trampert, and K. H. Ploog, Phys. Rev. B **72**, 045423 (2005).
[61]V. M. Kaganer, O. Brandt, H. Riechert, and K. K. Sabelfeld, Phys. Rev. B **80**, 033306 (2009).
[62]P. John, P. Vennéguès, H. Rotella, C. Deparis, C. Lichtensteiger, and J. Zúñiga Pérez, J. Appl. Phys. **129** (2021).
[63]M. Becht, F. Wang, J. G. Wen, and T. Morishita, J. Cryst. Growth **170**, 799–802 (1997).
[64]J. Bläsing, A. Krost, J. Hertkorn, F. Scholz, L. Kirste, A. Chuvilin, and U. Kaiser, J. Appl. Phys. **105**, 033504 (2009).
[65]M. W. Cho, A. Setiawan, H. J. Ko, S. K. Hong, and T. Yao, Semicond. Sci. Technol. **20**, S13 (2005).
[66]K. Zhang, Z. Xu, S. Zhang, H. Wang, H. Cheng, J. Hao, J. Wu, and F. Fang, Phys. B **600**, 412624 (2021).
[67]K. Sasaki, M. Higashiwaki, A. Kuramata, T. Masui, and S. Yamakoshi, J. Cryst. Growth **392**, 30–33 (2014).
[68]S. Krishna, Y. Lu, C.-H. Liao, V. Khandelwal, and X. Li, Appl. Surf. Sci. **599**, 153901 (2022).
[69]M. Grundmann, T. Böntgen, and M. Lorenz, Phys. Rev. Lett. **105**, 146102 (2010).

14 November 2023 01:39:54

© Author(s) 2023